

FaST: Efficient and Effective Long-Horizon Forecasting for Large-Scale Spatial-Temporal Graphs via Mixture-of-Experts

Yiji Zhao

Yunnan University
School of Information
Science and Engineering
Kunming, China
yjzhao@ynu.edu.cn

Ming Jin

Griffith University
Brisbane, Australia
mingjinedu@gmail.com

Zihao Zhong

Yunnan University
School of Information
Science and Engineering
Kunming, China
zhongzihao@stu.ynu.edu.cn

Yuxuan Liang

The Hong Kong University
of Science and Technology
(Guangzhou)
Guangzhou, China
yuxliang@outlook.com

Ao Wang

Yunnan University
School of Information
Science and Engineering
Kunming, China
wangao@stu.ynu.edu.cn

Haomin Wen

Carnegie Mellon University
Pittsburgh, United States
haominwe@andrew.cmu.edu

Hao Wu*

Yunnan University
School of Information
Science and Engineering
Kunming, China
haowu@ynu.edu.cn

Abstract

Spatial-Temporal Graph (STG) forecasting on large-scale networks has garnered significant attention. However, existing models predominantly focus on short-horizon predictions and suffer from notorious computational costs and memory consumption when scaling to long-horizon predictions and large graphs. Targeting the above challenges, we present **FaST**, an effective and efficient framework based on heterogeneity-aware Mixture-of-Experts (MoEs) for long-horizon and large-scale STG forecasting, which unlocks one-week-ahead (672 steps at a 15-minute granularity) prediction with thousands of nodes. FaST is underpinned by two key innovations. First, an adaptive graph agent attention mechanism is proposed to alleviate the computational burden inherent in conventional graph convolution and self-attention modules when applied to large-scale graphs. Second, we propose a new parallel MoE module that replaces traditional feed-forward networks with Gated Linear Units (GLUs), enabling an efficient and scalable parallel structure. Extensive experiments on real-world datasets demonstrate that FaST not only delivers superior long-horizon predictive accuracy but also achieves remarkable computational efficiency compared to state-of-the-art baselines. Source code is publicly available at: <https://github.com/yijizhao/FaST>.

CCS Concepts

• Information systems → Spatial-temporal systems.

*Hao Wu is the corresponding author.

Permission to make digital or hard copies of all or part of this work for personal or classroom use is granted without fee provided that copies are not made or distributed for profit or commercial advantage and that copies bear this notice and the full citation on the first page. Copyrights for components of this work owned by others than the author(s) must be honored. Abstracting with credit is permitted. To copy otherwise, or republish, to post on servers or to redistribute to lists, requires prior specific permission and/or a fee. Request permissions from permissions@acm.org.

KDD '26, Jeju Island, Republic of Korea

© 2026 Copyright held by the owner/author(s). Publication rights licensed to ACM.

Keywords

Long-Horizon Forecasting, Large-Scale Spatial-Temporal Graph, Mixture of Experts

1 Introduction

Spatial-Temporal Graph (STG) serves as a powerful data schema for modeling complex dependencies in urban sensing systems, where nodes represent sensors (e.g., traffic detectors, energy meters) and edges capture spatial relationships [21, 35]. Accurate long-horizon STG forecasting (e.g., days ahead) can shift urban management from reactive responses to proactive planning. For example, a seven-day electricity demand outlook allows renewable generation and storage to be scheduled ahead of peak loads. Such scenarios are typically coupled with two features: 1) a long forecasting horizon (e.g., 672 steps at 15-minute granularity covers one week) and 2) a large-scale graph (e.g., over thousands of nodes).

Extensive efforts have been made in STG forecasting, where most works focus on short-term forecasting (i.e., 12-step) in graphs with fewer than hundreds of nodes. Representative models build a Spatial-Temporal Graph Neural Networks (STGNNs), such as DCRNN [26] and STGCN [46], coupling Graph Neural Networks (GNNs) with sequence models to capture both the spatial and temporal dependencies. Later improvements incorporate graph attention [14, 15, 50], temporal transformers [15, 27], and neural graph ODEs [12] to boost short-term accuracy. However, those STGNNs suffer from quadratic complexity hidden in both spatial and temporal modules: GNNs and spatial/temporal attention incur $O(N^2)$ and $O(T^2)$ pairwise node/time-step interactions over N nodes and sequence length T , respectively. When N and T scale jointly, resource demands increase exponentially. To give a concrete example, we report the training cost vs. performance on a large-scale STG benchmark [32] in Figure 1, when confronted with 8,600 nodes and a 672-step prediction horizon (a practical setting in CA dataset), most representative STGNNs exhaust 48 GB of GPU memory, making them impractical to train and deploy in most GPU devices.

To elevate the STGNNs for large-scale and long-horizon forecasting, **a critical challenge is to achieve linear computational**

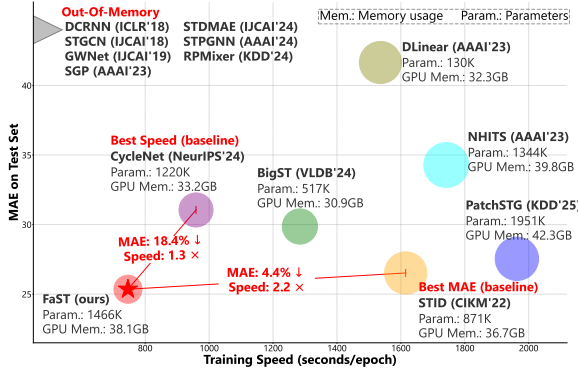


Figure 1: Efficiency-effectiveness comparison on large-scale STG benchmark (CA dataset; 8,600 nodes; 672-step prediction horizon). Smaller bubble means faster inference speed. The proposed FaST achieves the best performance and speed (both in training and inference).

complexity while retaining the rich spatial and temporal semantics required for long-horizon forecasting. Recent studies have explored two complementary directions to reduce pairwise node/time-step interactions, though promising, they still face major limitations in both performance and efficiency.

Spatially, existing efficient methods can be broadly categorized into *structure-aware* and *structure-free* approaches. Structure-aware methods leverage the explicit graph topology to reduce spatial interactions through techniques such as sparse aggregation (e.g., SGP [7]), neighbor sampling (e.g., SAGDFN [20]), and graph partitioning (e.g., PatchSTG [11]). However, these approaches often discard long-range dependencies and heavily rely on an accurate graph structure (which may not always be available in real-world scenarios). To circumvent this, structure-free methods avoid using graph structure and instead rely on node embeddings and feature-mixing mechanisms. For example, BigST [17] adopts linear attention to bypass pairwise node computation; RPMixer [45] employs random projection and MLPs to facilitate efficient spatial fusion; and STID [37] eliminates spatial interactions by encoding spatial identity with positional embeddings. While these techniques reduce the complexity from $O(N^2)$ to $O(N \cdot \phi)$, where $\phi < N$ is a tunable factor depending on the implementation and hyperparameters (e.g., sampled neighbors, feature dimension, or partition granularity), they often oversimplify the interaction operation, which can dilute meaningful relationships, introduce irrelevant noise, and therefore lead to significant loss of spatial semantics.

Temporally, two main strategies have emerged: *sparse/linear attention mechanisms* and *temporal pattern compression methods*. The former, adopted in models like Airformer [27], SAGDFN [20], and BigST [17], aims to alleviate the quadratic cost of temporal attention by approximating it with lower-complexity variants. The latter strategy, employed in methods such as CycleNet [28] and STID [37], compresses long historical sequences into a compact low-dimensional embedding per node, effectively removing explicit pairwise interactions across time steps. For example, STID directly compresses the T -step history into a dense embedding via a simple

linear projection, while CycleNet encodes periodicity by learning a fixed-length recurrent cycle template, both avoiding explicit token-wise temporal interactions. However, due to sharing a single compression module across both spatial units and temporal segments, these methods effectively impose a one-size-fits-all scheme, often homogenizing temporal representations and ignoring heterogeneous temporal patterns across nodes and time periods, risking the loss of temporal diversity and fine-grained dynamics and thus compromising expressiveness and generalization, especially for long-range forecasting tasks.

To address the above limitations, we propose **FaST**, a Fast long-horizon forecasting framework for large-scale Spatial-Temporal graphs. FaST is a heterogeneity-aware parallelized Mixture-of-Experts (MoE) networks. Firstly, an MoE-based temporal compression input module projects historical sequences into a low-dimensional dense embedding, improving computational efficiency and preventing memory explosion concerning the historical input length. To mitigate the information loss and representation homogenization induced by compression, we introduce a heterogeneity-aware router that dynamically selects expert-specific compression pathways across nodes and time periods, thereby extracting diversified temporal features. Furthermore, an expert-concurrent mechanism based on Gated Linear Units (GLUs) is proposed to achieve efficient feature extraction. Secondly, an adaptive graph agent attention module is introduced, where a agent tokens ($a \ll N$) are learned to reduce the long-range spatial interaction complexity from $O(N^2)$ to $O(Na)$. Finally, a multi-layer MoE network is built to extract diverse spatial features.

The main contributions are summarized as follows:

- **Framework:** We propose FaST, the first framework for long-horizon and large-scale STG forecasting that unlocks the prediction span to one week and node size to tens of thousands within a tolerable time.
- **Parallelized Mixture-of-Experts:** A novel heterogeneity-aware router and a parallel GLU-MoE module are proposed, which can efficiently and effectively extract diverse spatial and temporal features based on node heterogeneity.
- **Linear Complexity:** With the Temporal Compression Input with MoE module and the adaptive graph agent attention module, FaST achieves linear computational complexity w.r.t. the number of nodes while maintaining the ability of long-range spatial-temporal dependency modeling.
- **Effectiveness:** Extensive experiments on the large-scale STG forecasting benchmark, as shown in Figure 1, show that FaST exhibits superior long-range forecast performance, reducing 4.4% ~ 18.4% in prediction error, and is 1.3 \times ~ 2.2 \times faster than the SOTA model, demonstrating significant computational efficiency.

2 Problem Formulation

Given N spatial nodes (e.g., sensors, regions), we denote measurements (e.g., traffic flow) recorded at N nodes over T sequential time steps by $\mathbf{X}_t = [\mathbf{x}_{t-T+1}, \dots, \mathbf{x}_t] \in \mathbb{R}^{N \times T}$. The relationships among spatial locations are represented using an undirected graph $\mathcal{G} = (\mathcal{V}, \mathcal{E})$, where $\mathcal{V} = \{v_i | i \in 1, 2, \dots, N\}$ is the set of N nodes, and $\mathcal{E} = \{(v_i, v_j) | v_i, v_j \in \mathcal{V}\}$ is the set of edges among nodes. \mathcal{E} can be derived using a predefined topology structure (e.g., a road

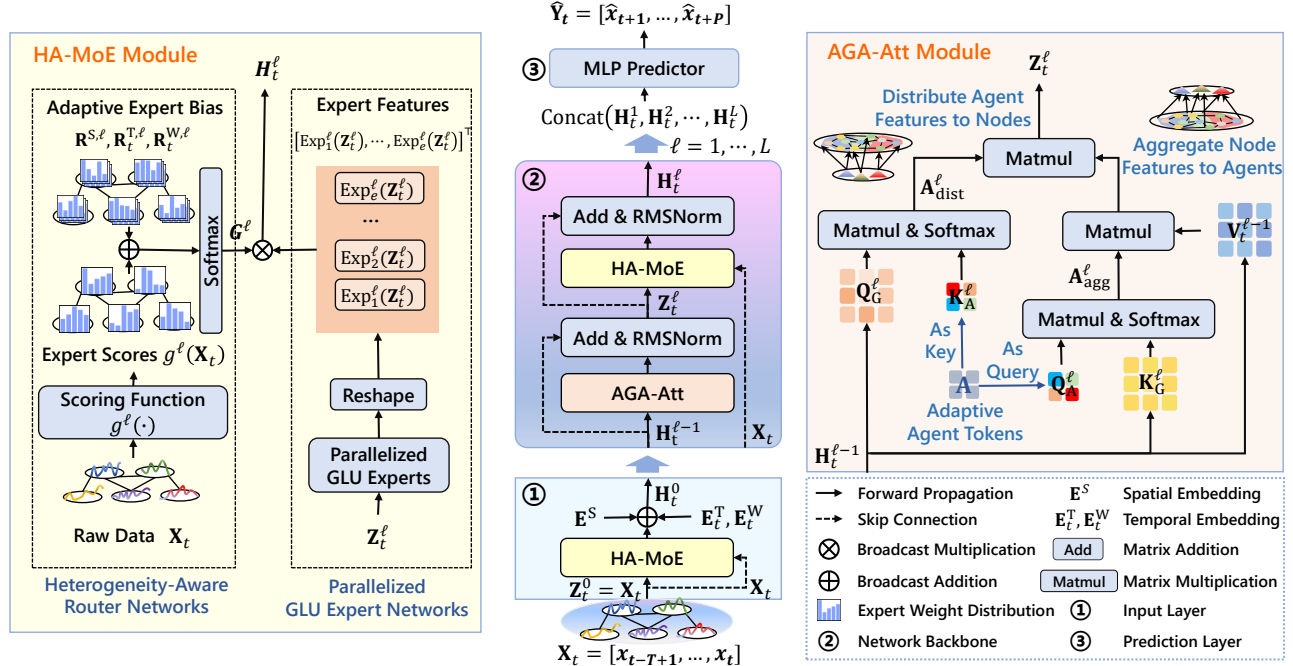


Figure 2: Architecture of FaST. The middle part illustrates the workflow: the input sequence X_t is first embedded and fed into L stacked backbone blocks, and the resulting representations are concatenated and passed to an MLP predictor to generate \hat{Y}_t .

network) or can be learned adaptively from the data in an end-to-end manner. In this work, a set $\mathcal{U} = \{u_i | i \in 1, 2, \dots, a\}$ of ($a \ll N$) learnable agent tokens is introduced, whose relationships $\mathcal{E}' = \{(v_i, u_j) | v_i \in \mathcal{V}, u_j \in \mathcal{U}\}$ with the original nodes are obtained through interaction. Thus, the graph becomes $\mathcal{G} = (\mathcal{V} \cup \mathcal{U}, \mathcal{E}')$. The goal of a general STG forecasting is to predict the future measurements $\mathbf{Y}_t = [\mathbf{x}_{t+1}, \dots, \mathbf{x}_{t+P}] \in \mathbb{R}^{N \times P}$ over P time steps by learning a mapping $f_{\mathcal{G}}$ as follows:

$$\hat{Y}_t = f_{\mathcal{G}}(\mathbf{X}_t; \Theta), \quad (1)$$

where \hat{Y} is the prediction of future traffic flows, and Θ is the set of all trainable parameters of $f_{\mathcal{G}}$.

3 Methodology

The architecture of FaST, as shown in Figure 2, consists of three components: ① Input Layer: The raw sequence \mathbf{X}_t is first mapped into dense representations via a Heterogeneity-aware MoE (HA-MoE) module, and then augmented with adaptive spatial and temporal embeddings. ② Network Backbone: FaST stacks L residual blocks. In each block, a Adaptive Graph Agent Attention (AGA-Att) module first summarizes node features into a small set of agent tokens and redistributes the aggregated information back to all nodes; HA-MoE is then applied to perform heterogeneity-aware enhancement. ③ Prediction Layer: The outputs from all layers are concatenated and passed to an MLP head to produce the final forecasts.

3.1 Network Backbone

FaST uses a transformer-like stacked block to perform spatial-temporal feature extraction. Specifically, the proposed AGA-Att is

used to replace traditional self-attention, and the proposed HA-MoE is then employed instead of the Feed-Forward Network (FFN) layer to perform efficient feature transformation. The backbone of FaST is a stack of L residual blocks, shown as follows:

$$\begin{aligned} \mathbf{H}_t^{\ell} &= \text{RMSNorm}(\text{HA-MoE}(\mathbf{Z}_t^{\ell}, \mathbf{X}_t) + \mathbf{Z}_t^{\ell}) \\ \mathbf{Z}_t^{\ell} &= \text{RMSNorm}(\text{AGA-Att}(\mathbf{H}_t^{\ell-1}) + \mathbf{H}_t^{\ell-1}), \end{aligned} \quad (2)$$

where $\text{RMSNorm}(\cdot)$ is a root mean square layer normalization operation [48]. The input to the first layer ($\ell = 1$) of the network is initialized with the features in Eq. (4).

3.2 MoE-based Temporal Compression Input

Long-horizon forecasting requires capturing fine-grained historical dependencies while remaining computationally scalable. To reconcile accuracy and efficiency, we introduce an MoE-based temporal compression module that projects the T -step raw sequence into a compact dense embedding using multiple learnable projection experts. Unlike one-size-fits-all compression, a heterogeneity-aware router dynamically selects expert-specific compression pathways across nodes and time periods, mitigating representation homogenization and alleviating information loss under compression.

Specifically, given an input $\mathbf{X}_t \in \mathbb{R}^{N \times T}$, use a HA-MoE module to reduce the information from T time steps to a d -dimensional dense embedding as follows:

$$\tilde{\mathbf{H}}_t = \text{HA-MoE}(\mathbf{Z}_t^0, \mathbf{X}_t) \in \mathbb{R}^{N \times d}, \quad (3)$$

where $\mathbf{Z}_t^0 = \mathbf{X}_t$. In addition, trainable spatial and temporal embeddings are added to the feature to identify the spatial and temporal

positions, shown as follows:

$$\mathbf{H}_t^0 = \bar{\mathbf{H}}_t \oplus \mathbf{E}_t^S \oplus \mathbf{E}_t^D \oplus \mathbf{E}_t^W \in \mathbb{R}^{N \times d}, \quad (4)$$

where \oplus is a broadcast addition operation, $\mathbf{E}_t^S \in \mathbb{R}^{N \times d}$ encodes the structural/positional priors of nodes, and $\mathbf{E}_t^D \in \mathbb{R}^{1 \times d}$ and $\mathbf{E}_t^W \in \mathbb{R}^{1 \times d}$ encode the position of the time step t within a day and a week, respectively. The aforementioned \mathbf{E}_t^S , \mathbf{E}_t^D , and \mathbf{E}_t^W are initialized as trainable embeddings and optimized alongside the model.

3.3 Heterogeneity-Aware MoE (HA-MoE)

To manifest the impact of heterogeneity on prediction accuracy, it is necessary to characterize this difference through a variety of representations. The mixture of experts architecture is a neural network design that leverages multiple specialized sub-networks (called "experts") to handle different parts of the input data [18]. A gating network dynamically routes each input to the most relevant experts [6], enabling the model to scale efficiently and specialize in diverse tasks [39, 52]. In FaST, the MoE architecture is used to extract diverse features.

Load Balancing Problem. Despite the scalability of MoE architectures, they often suffer from load imbalance, where a small number of experts dominate routing decisions, while others remain underutilized, a phenomenon known as expert weight polarization [2]. Such an imbalance can diminish the model's effective capacity and destabilize training processes. Previous approaches address this issue by implementing auxiliary load balancing losses or capacity constraints [38, 39]. However, these methods often increase training complexity or restrict the flexibility inherent in expert specialization. FaST tackles this challenge through a Heterogeneity-Aware Router (HA-Router) network and a dense MoE design, enabling all experts to contribute to the forward computation.

Heterogeneity-Aware Router Networks (HA-Router). It avoids expert polarization by exploiting the spatial-temporal heterogeneity of the input. Specifically, HA-Router measures the correlation between experts and features by absorbing raw time-series patterns and injecting adaptive spatial and temporal expert biases. This heterogeneity-aware routing design forces nodes to select experts relevant to themselves rather than concentrating on a single expert. Given e experts and node features $\mathbf{Z}_t^\ell \in \mathbb{R}^{N \times d}$, the expert weight is calculated as follows:

$$\begin{aligned} \mathbf{G}^\ell &= \text{softmax} \left(g^\ell(\mathbf{X}_t) \oplus \mathbf{R}_t^{\text{S},\ell} \oplus \mathbf{R}_t^{\text{T},\ell} \oplus \mathbf{R}_t^{\text{W},\ell} \right) \in \mathbb{R}^{N \times e} \\ g^\ell(\mathbf{X}_t) &= \mathbf{X}_t \mathbf{W}^\ell \in \mathbb{R}^{N \times e}, \end{aligned} \quad (5)$$

where \oplus is a broadcast addition operation, $g^\ell(\cdot)$ is a scoring function used to calculate expert scores, and $\mathbf{W}^\ell \in \mathbb{R}^{T \times e}$ is a trainable parameter. $\mathbf{R}^{\text{S}} \in \mathbb{R}^{N \times e}$ and $\mathbf{R}^{\text{T}}_t, \mathbf{R}^{\text{W}}_t \in \mathbb{R}^{1 \times e}$ are adaptive spatial and temporal expert biases obtained via trainable parameters. Specifically, \mathbf{R}^{S} captures the expert bias on the spatial locations while \mathbf{R}^{T}_t and \mathbf{R}^{W}_t encode the expert bias on the temporal horizons (e.g., time of day and day of week). Finally, the weight distribution $\mathbf{G}^\ell \in \mathbb{R}^{N \times e}$ is used to assign weights to the experts and aggregate their representations, shown as follows:

$$\text{HA-MoE}(\mathbf{Z}_t^\ell, \mathbf{X}_t) = \sum_{i=1}^e \mathbf{G}^\ell[:, i] \otimes \text{Exp}_i(\mathbf{Z}_t^\ell), \quad (6)$$

where \otimes is a broadcast multiplication, and $\text{Exp}_i(\mathbf{Z}_t^\ell) \in \mathbb{R}^{N \times d}$ is i -th expert's output. This router adapts to input variations, making MoE suitable for heterogeneous data. Experts can specialize in different aspects of the data, improving model performance on diverse tasks.

Parallelized GLU Expert Networks. For the selection of experts, existing works generally use FFNs. However, FFNs with a multi-layer structure often require complex mechanisms and high costs to achieve parallelism (e.g., assigning experts to different computing units). A promising alternative is to use linear units as experts, which have good computational efficiency and parallelism. To maintain model capacity and its ability to model nonlinear relationships, GLUs [8] are used as experts in FaST.

Generally, each expert $\text{Exp}_i(\mathbf{Z}_t^\ell) \in \mathbb{R}^{N \times d}$ is an instance of a GLU:

$$\begin{aligned} \text{Exp}_i(\mathbf{Z}_t^\ell) &= \text{GLU}_i(\mathbf{Z}_t^\ell) \\ &= \sigma(\mathbf{Z}_t^\ell \mathbf{W}_{i,2}^\ell + \mathbf{b}_{i,2}^\ell) \odot (\mathbf{Z}_t^\ell \mathbf{W}_{i,1}^\ell + \mathbf{b}_{i,1}^\ell), \end{aligned} \quad (7)$$

where \odot denotes the element-wise multiplication, σ denotes the sigmoid activation function, $\mathbf{W}_{i,1}^\ell, \mathbf{W}_{i,2}^\ell \in \mathbb{R}^{d \times d}$ and $\mathbf{b}_{i,1}^\ell, \mathbf{b}_{i,2}^\ell \in \mathbb{R}^d$ are trainable parameters. However, the instances in Eq. 7 are inefficient, similar to FFNs. Therefore, an efficient parallel computing mechanism for GLU experts is constructed as follows:

$$\begin{aligned} [\text{Exp}_1(\mathbf{Z}_t^\ell), \dots, \text{Exp}_e(\mathbf{Z}_t^\ell)]^\top &= \text{Reshape}(\sigma(\mathbf{F}_1^\ell) \odot \mathbf{F}_2^\ell) \\ \mathbf{F}_1^\ell, \mathbf{F}_2^\ell &= \text{Split}(\mathbf{Z}_t^\ell \mathbf{W}_F^\ell + \mathbf{b}_F^\ell), \end{aligned} \quad (8)$$

where \top indicates a transpose operation. $\text{Reshape}(\cdot)$ and $\text{Split}(\cdot)$ are tensor reshaping and splitting operations, respectively. $\mathbf{W}_F^\ell \in \mathbb{R}^{d \times 2ed}$ and $\mathbf{b}_F^\ell \in \mathbb{R}^{2ed}$ are trainable parameters. As shown in Eq. (8), the linear transformation calculations of experts are merged into a linear layer consisting of \mathbf{W}_F^ℓ and \mathbf{b}_F^ℓ . The output of the linear layer is split into two parts ($\mathbf{F}_1^\ell, \mathbf{F}_2^\ell \in \mathbb{R}^{N \times d}$) to calculate the output of GLUs. Finally, the output $[\text{Exp}_1(\mathbf{Z}_t^\ell), \dots, \text{Exp}_e(\mathbf{Z}_t^\ell)]^\top \in \mathbb{R}^{N \times e \times d}$ of multiple GLU experts can be calculated simultaneously by reshaping one integrated GLU expert's output from $N \times ed$ to $N \times e \times d$. Therefore, our model can achieve good parallel processing on a single computing unit, avoiding the additional cost of complex parallel mechanisms.

For clarity, the proposed HA-MoE module is denoted as:

$$\text{HA-MoE}(\mathbf{Z}_t^\ell, \mathbf{X}_t) = \mathbf{G}^\ell \otimes [\text{Exp}_1(\mathbf{Z}_t^\ell), \dots, \text{Exp}_e(\mathbf{Z}_t^\ell)]^\top, \quad (9)$$

where \otimes is a broadcast multiplication, and $\mathbf{G}^\ell \in \mathbb{R}^{N \times e}$ is the weight of experts generated by the HA-Router Network (Eq. (5)).

3.4 Adaptive Graph Agent Attention (AGA-Att)

The high complexity of GCNs on raw graph structures prevents a large number of spatial-temporal methods from running on large-scale STGs. Inspired by [16], FaST uses a set of adaptive agent tokens $\mathcal{U} = \{u_i | i \in 1, 2, \dots, a\}$ as intermediaries to effectively aggregate and distribute information, capturing long-range spatial dependencies. Specifically, an adaptive embedding token is generated for each agent token, and the embeddings of all agent tokens are denoted as $\mathbf{A} \in \mathbb{R}^{a \times d}$. Below, the interaction details between agent tokens and graph node tokens are introduced.

Node-to-Agent Aggregation Attention: Each agent token queries all graph node tokens to aggregate long-range spatial information. Concretely, the attention weights from agent queries to

graph keys are computed as

$$\mathbf{A}_{\text{agg}}^{\ell} = \text{Softmax} \left(\frac{\mathbf{Q}_A^{\ell} \mathbf{K}_G^{\ell \top}}{\sqrt{d}} \right), \quad \mathbf{Q}_A^{\ell} = \mathbf{A} \mathbf{W}_{\text{agg}}^{\ell,1}, \quad \mathbf{K}_G^{\ell} = \mathbf{H}_t^{\ell} \mathbf{W}_{\text{agg}}^{\ell,2}, \quad (10)$$

where, $\mathbf{W}_{\text{agg}}^{\ell,1}, \mathbf{W}_{\text{agg}}^{\ell,2} \in \mathbb{R}^{d \times d}$ are trainable weight matrices.

Agent-to-Node Distribution Attention: Each graph node token queries the agent tokens to obtain the summarized global context and distributes it back to nodes. Specifically, the attention weights from node queries to agent keys are computed as

$$\mathbf{A}_{\text{dist}}^{\ell} = \text{Softmax} \left(\frac{\mathbf{Q}_G^{\ell} \mathbf{K}_A^{\ell \top}}{\sqrt{d}} \right), \quad \mathbf{Q}_G^{\ell} = \mathbf{H}_t^{\ell} \mathbf{W}_{\text{dist}}^{\ell,1}, \quad \mathbf{K}_A^{\ell} = \mathbf{A} \mathbf{W}_{\text{dist}}^{\ell,2}, \quad (11)$$

where $\mathbf{W}_{\text{dist}}^{\ell,1}, \mathbf{W}_{\text{dist}}^{\ell,2} \in \mathbb{R}^{d \times d}$ are trainable weight matrices.

The final output of AGA-Att is as follows:

$$\begin{aligned} \text{AGA-Att}(\mathbf{H}_t^{\ell-1}) &= \mathbf{A}_{\text{dist}}^{\ell} (\mathbf{A}_{\text{agg}}^{\ell} \mathbf{V}_t^{\ell-1}) \\ \mathbf{V}_t^{\ell-1} &= \mathbf{H}_t^{\ell-1} \mathbf{W}_V^{\ell} \end{aligned} \quad (12)$$

where $\mathbf{W}_V^{\ell} \in \mathbb{R}^{d \times d}$ is the trainable value projection matrix. The AGA-Att mechanism can be viewed as a low-rank spatial interaction bottleneck: graph tokens first project information to a small set of shared agent tokens and then receive redistributed summaries from them. Apparently, by reducing the number of direct interactions between input tokens, the above mechanism can lower the computational cost from $O(N^2)$ to $O(Na)$, where N is the number of input tokens and a is the number of agent tokens ($a \ll N$). This design is most effective when node-level temporal behaviors contain shared modes (i.e., spatial redundancy), so that the node representation manifold can be well-approximated by a limited number of latent prototypes. When spatial redundancy is weaker, increasing the number of agents can partially compensate, at the expense of higher $O(Na)$ cost.

3.5 Prediction Layer

In the prediction phase, a multilayer perceptron (MLP) is used to generate future multi-step results directly. Specifically, the features from the L layers are concatenated as follows:

$$\mathbf{U}_t = \text{Concat} (\mathbf{H}_t^1, \mathbf{H}_t^2, \dots, \mathbf{H}_t^L), \quad (13)$$

where $\text{Concat}(\cdot)$ denotes the concatenate operation. Then $\mathbf{U}_t \in \mathbb{R}^{N \times Ld}$ is fed into the multilayer perceptron to generate future predictions as follows:

$$\hat{\mathbf{Y}}_t = (\text{ReLU} (\mathbf{U}_t \mathbf{W}_1 + \mathbf{b}_1)) \mathbf{W}_2 + \mathbf{b}_2, \quad (14)$$

where $\mathbf{W}_1 \in \mathbb{R}^{Ld \times Ld}, \mathbf{W}_2 \in \mathbb{R}^{Ld \times P}, \mathbf{b}_1 \in \mathbb{R}^{Ld}$, and $\mathbf{b}_2 \in \mathbb{R}^P$ are trainable parameters.

3.6 Loss Function

The Huber loss is chosen as the loss function because it is robust to the regression problem [19]. It is defined as follows:

$$\mathcal{L}(y, \hat{y}) = \begin{cases} \frac{1}{2}(y - \hat{y})^2 & \text{for } |y - \hat{y}| \leq \delta \\ \delta|y - \hat{y}| - \frac{1}{2}\delta^2, & \text{otherwise,} \end{cases} \quad (15)$$

where y and \hat{y} are the observed and predicted values, and δ is a threshold (1 by default). The objective function is shown below:

$$\arg \min_{\Theta} \sum_{n=1}^N \sum_{p=1}^P \mathcal{L} (\mathbf{Y}_t[n, p], \hat{\mathbf{Y}}_t[n, p]). \quad (16)$$

3.7 Complexity Analysis

The computational complexity of the FaST is primarily driven by MoE and attention modules. Since the time dimension is compressed, the space required to store the spatial-temporal hidden representation is $O(Nd)$, and the time complexity of the compression process is $O(Td)$. On this basis, the time and space complexity of calculating and storing e expert representations is $O(ed^2)$ and $O(Ned)$, respectively. For agent attention, the time and space complexity of calculating and storing the attention distribution are $O(Nad)$ and $O(Na)$, respectively. Overall, the temporal complexity of FaST is $O(Td + Nad)$ and the spatial complexity is $O(Ned + Na)$, which are linearly related to the number of time steps and nodes, and thus have good scalability. In addition, since the spatial agent tokens avoid pairwise spatial interactions between nodes, FaST can achieve good parallelism across multiple computing units.

4 Experiments

In this section, we evaluate FaST on benchmark datasets. We first introduce the datasets, metrics, and baselines, and then report the main results, ablations, hyperparameter sensitivity, and computational cost. We further provide case studies to show how the MoE design captures heterogeneity across nodes and time periods.

4.1 Experimental Settings

Datasets. We conduct experiments using the LargeST dataset [32], which contains four traffic subset: SD (San Diego), GBA (Greater Bay Area), GLA (Greater Los Angeles), and CA (California). Detailed statistics are provided in Table 1. Each subset is split into 6:2:2 training, validation, and test sets in chronological order.

Table 1: Dataset statistics.

Data	#Nodes	Granularity	Time span	Std	Mean	#Samples
SD	716	15 minute	2019 (full year)	184.02	244.31	24.5M~25.0M
GBA	2,352	15 minute	2019 (full year)	166.67	239.82	80.6M~82.1M
GLA	3,834	15 minute	2019 (full year)	187.77	276.82	131.4M~133.8M
CA	8,600	15 minute	2019 (full year)	177.12	237.39	294.7M~300.1M

Evaluation Metrics. Model performance is evaluated using widely adopted error metrics, including MAE, RMSE, and MAPE, where lower values indicate better predictive accuracy. In addition, we report the coefficient of determination (R^2) to quantify how well the predicted sequences explain the variance of the ground-truth series (higher is better).

Baselines. To ensure representativeness, timeliness, and competitiveness, we consider two groups of baselines: (i) **temporal-centric methods** that model time-series dynamics without explicit spatial structures, including *DLinear* [47]: decomposes a series into trend and residual components and models them with lightweight linear projections; *NHITS* [3]: performs multi-rate processing with

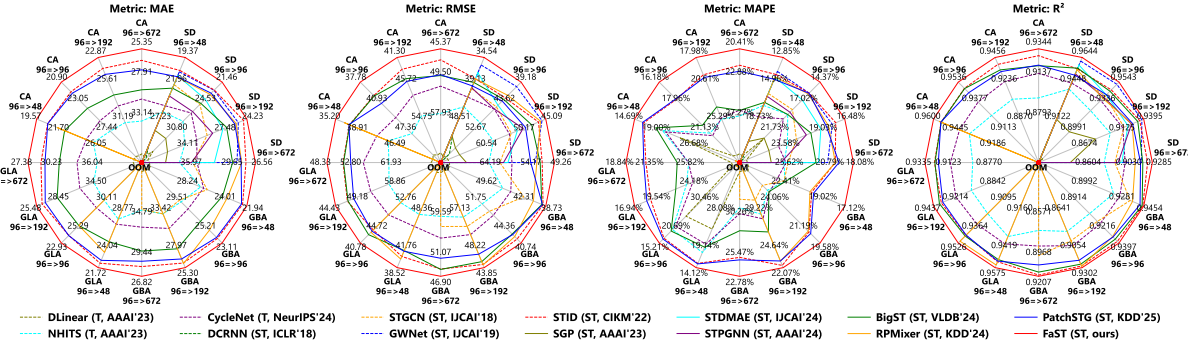


Figure 3: Long-horizon forecasting performance comparison. "96=>672" denotes 672 steps ahead forecasting based on the past 96 time steps. "T" refers to temporal-centric methods, while "ST" denotes spatial-temporal-centric methods. FaST achieved the best performance on 16 prediction tasks.

hierarchical interpolation for multihorizon forecasting; and *CycleNet* [28]: uses a cycle-consistency objective to better capture periodic patterns. **(ii) spatial-temporal-centric methods**, including *DCRNN* [26]: combines diffusion graph convolution with a sequence-to-sequence architecture for spatiotemporal modeling; *STGCN* [46]: models spatiotemporal correlations via graph and temporal convolutions; *GWNet* [44]: integrates gated temporal convolutions with adaptive graph convolutions; *SGP* [7]: uses randomized recurrent components with GNNs for scalable learning on large graphs; *STID* [37]: augments simple MLPs with spatial/temporal identity cues to mitigate sample indistinguishability; *STDMAE* [13]: applies decoupled masked autoencoding to reconstruct sequences along spatial and temporal dimensions; *BigST* [17]: introduces long-sequence feature extraction and linearized global spatial convolution for large-scale networks; *RPMixer* [45]: leverages random projections and a mixer architecture to build a lightweight model; *STPGNN* [22]: selects pivotal nodes and uses parallel convolutions to capture spatiotemporal dependencies in traffic data; and *PatchSTG* [11]: adopts KDTree-based irregular patching to reduce Transformer cost while preserving fidelity and interpretability.

Implementation Details. The task is to forecast the next {48, 96, 192, 672} horizons based on observations from the 96 historical time steps (i.e., 1 day). To ensure fairness and reproducibility, all experiments are implemented on the BasicTS [36] benchmark framework. All models share the same hidden dimension (#dim=64), are trained for at most 50 epochs with early stopping, and other baseline hyperparameters follow their official BasicTS configurations. FaST uses a single fixed configuration across all datasets (#experts=8, #layers=3, #agents=32, #dim=64), selected for efficiency rather than per-dataset tuning. We train FaST with Adam using an initial learning rate of 0.002, decayed by a factor of 0.5 every 10 epochs. All experiments are conducted on an AMD EPYC 7532 @2.40GHz CPU, an NVIDIA RTX A6000 GPU (48GB), and 128GB RAM.

4.2 Performance Comparison

Figure 3 and Table 6 (See Appendix) present the long-horizon forecasting results for MAE, RMSE, MAPE, and R^2 across specific horizons of 48, 96, 192, and 672.

On the SD dataset, DLinear demonstrates the poorest performance due to its limited capacity for nonlinear modeling. Compared to purely linear baselines (e.g., DLinear), NHITS and CycleNet introduce nonlinear transforms that can better capture non-stationary and multi-scale temporal patterns. Specifically, NHITS employs a hierarchical structure with multiple sampling rates to capture patterns across various time scales. CycleNet, on the other hand, is explicitly designed to model cyclical patterns. These temporal-centric methods cannot effectively leverage spatial correlation, resulting in inferior performance. When modeling spatial-temporal correlations using graphs and convolutions, DCRNN underperforms compared to STGCN, GWNet, and STPGNN. All leverage more advanced GNN architectures, with STGCN excelling in short-range scenarios, GWNet performing better in long-horizon cases, and STPGNN identifying and capturing the spatial-temporal dependencies of pivotal nodes. SGP fails to match its performance due to its less sophisticated approach to capturing spatial dependencies.

For large-scale modeling, BigST, STID, RPMixer, and PatchSTG show improved prediction accuracy, but some methods face scalability challenges on larger datasets. For instance, STGCN and STPGNN cannot complete training within tolerable time frames on GLA/CA, and RPMixer encounters memory limitations on GLA (192-step) and CA (96-step). Consequently, we evaluate only scalable methods, DLinear, NHITS, CycleNet, BigST, STID, PatchSTG, and RPMixer (where feasible), on the larger datasets. The performance trends remain consistent across all datasets: prediction accuracy degrades as horizon length increases. Basically, STID, PatchSTG, and RPMixer outperform BigST on all horizons, confirming their merits in addressing scalability bottlenecks.

Regarding FaST, it consistently outperforms all baselines across every metric, horizon, and dataset. On SD, it achieves average improvements of 4.73%, 2.36%, 8.35%, and 0.34% in MAE, RMSE, MAPE, and R^2 , respectively (vs. best baselines). Significant MAE/MAPE improvements are also observed on GBA (e.g., 1.66%~13.40%), GLA (1.94%~8.85%), and CA (3.67%~10.06%). Despite comparable parameter counts to STID, FaST delivers superior performance in all scenarios. Critically, its memory complexity scales linearly with nodes, enabling seamless application to the largest dataset.

4.3 Ablation Study

In this section, we conducted ablation experiments by removing different components of the FaST model on the four datasets to validate the contribution of each component. For a systematic evaluation, we defined four variants of FaST: a) **w/ LinearInput**: MoE-enhanced input layer is replaced with a linear layer; b) **w/o HA-MoE**: The HA-MoE module is removed and replaced with GLU; c) **w/o HA-Router**: The heterogeneity-aware router module is removed, and the expert weight distribution is predicted using the hidden representation output by the previous layer; d) **w/o AGA-Att**: The adaptive graph agent attention is removed.

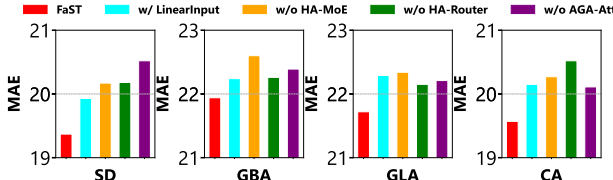


Figure 4: Ablation study of FaST components.

As shown in Figure 4, the complete FaST outperforms all variants on all datasets, validating the effectiveness of each module. Specifically, the *w/ LinearInput* shows a significant performance drop on both the SD and GLA datasets, indicating that the MoE-enhanced input layer is crucial for capturing complex features. The *w/o HA-MoE* exhibits the most pronounced performance decline, especially on GBA, demonstrating the core role of the MoE module in the model. The performance of *w/o HA-Router* and *w/o AGA-Att* also significantly decreases, indicating that the heterogeneity-aware router and agent attention modules contribute importantly to improving model performance. In conclusion, each component of FaST plays a positive role in the model’s performance, and its complete design achieves optimal performance in complex tasks.

Expert Component Comparison. A standard MoE layer assigns every token to one or more FFNs. To reduce latency without sacrificing quality, we substitute each FFN expert with a GLU-based expert. Empirically, GLU-Experts match the accuracy of FFN-Experts (Table 2) while yielding a 1.4x speed-up in wall-clock time.

Table 2: FaST with GLU-Expert vs. FFN-Expert. Notes: GPU memory usage (G.: GB), number of parameters (P.: K), training time (T.: second/epoch), and inference time (I.: second).

Data	Method	Performance			Efficiency			
		MAE	RMSE	MAPE	G.	P.	T.	I.
SD	FFN-Expert	19.41	34.15	12.80%	2.5	532	15	2
	GLU-Expert	19.37	34.54	12.85%	1.9	549	12	2
GBA	FFN-Expert	21.99	38.97	17.12%	6.9	689	48	9
	GLU-Expert	21.94	38.73	17.12%	5.0	706	36	8
GLA	FFN-Expert	21.57	38.26	13.95%	10.7	832	90	15
	GLU-Expert	21.72	38.52	14.12%	7.6	848	68	14
CA	FFN-Expert	20.35	36.77	15.58%	23.2	1289	225	37
	GLU-Expert	19.57	35.20	14.69%	17.2	1306	158	32

4.4 Hyperparameter Sensitivity

As illustrated in Figure 5, we conduct a sensitivity analysis on four critical hyperparameters that significantly influence the model’s performance: the number of experts (#experts), the number of backbone layers (#layers), the number of agent tokens in the agent-attention mechanism (#agents), and the feature dimension (#dimension).

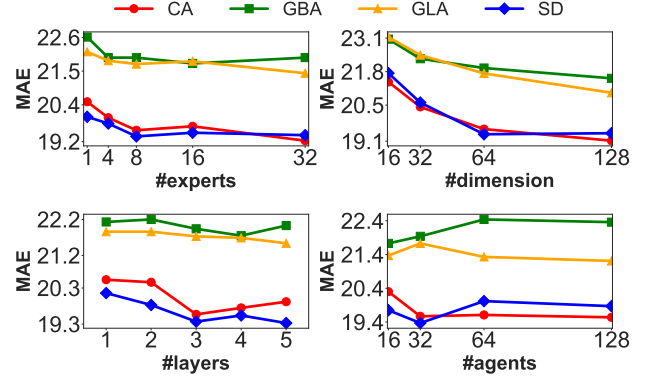


Figure 5: Visualization of hyperparameter sensitivity.

#experts. The optimal number of experts is 8 for CA/SD and 32 for GBA/GLA. Reducing the number of experts to 4 leads to a notable decline in performance, highlighting the importance of multiple experts in effectively modeling heterogeneity. While increasing the number of experts beyond the optimal values may yield marginal performance improvements, the associated computational costs may outweigh the benefits.

#dimension. The dimensionality of node embeddings is a crucial hyperparameter that significantly influences model cost, as the majority of the model’s parameters are determined by the number of nodes and the embedding dimension. Increasing the embedding dimension enhances the model’s ability to represent nodes, enabling the capture of more nuanced features. However, this improvement exhibits diminishing returns; for instance, increasing the dimension beyond 64 results in negligible changes in prediction accuracy.

#layers. This parameter directly impacts the computational complexity and the number of model parameters. The optimal configuration, however, depends on the dataset size. For the CA and SD datasets, 3 layers achieve the best prediction accuracy, with additional layers leading to overfitting and reduced performance. In contrast, the GBA and GLA datasets benefit from a deeper architecture, with 4 or 5 layers providing a more stable and effective representation learning capacity.

#agents. We evaluate the agent-attention mechanism with varying numbers of agent tokens: {16, 32, 64, 128}. Setting this parameter to 16 or 32 generally delivers robust performance. This range strikes a balance between prediction accuracy and computational efficiency, making it a practical choice for most scenarios.

4.5 Model Efficiency Comparison

Figure 6 summarizes the computational efficiency trends across horizons and datasets, while Tables 3 and 4 report the corresponding

computational cost in terms of GPU memory usage (G.: GB) and parameter count (P.: K).

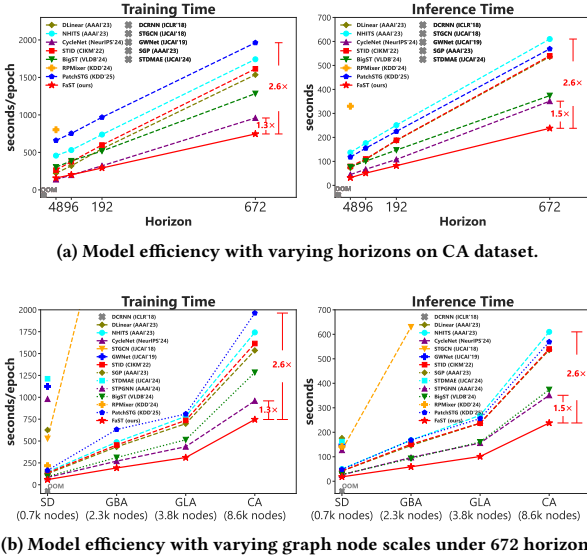


Figure 6: Model efficiency comparison.

Table 3: Computational cost across forecasting horizons on the CA dataset. Notes: batch size (B.S.), GPU memory usage (G.: GB), and number of parameters (P.: K).

Method	96=>48			96=>96			96=>192			96=>672		
	B.S.	G.	P.	B.S.	G.	P.	B.S.	G.	P.	B.S.	G.	P.
DLinear	64	3.3	9	64	5.5	19	64	10.3	37	64	32.3	130
NHITS	64	11.6	983	64	13.5	1,011	64	17.2	1,066	64	39.8	1,344
CycleNet	64	5.8	900	64	7.0	925	64	11.6	974	64	33.2	1,220
BigST	64	32.4	357	64	32.8	369	64	38.1	394	32	30.9	517
STID	64	7.9	771	64	10.0	778	64	15.0	794	64	36.7	871
RPMixer	64	27.5	7,813	/	/	/	/	/	/	/	/	/
PatchSTG	32	28.8	1,850	32	29.2	1,858	32	31.4	1,874	32	42.3	1,951
FaST	64	17.2	1,306	64	18.8	1,318	64	21.1	1,343	64	38.1	1,466

†Methods not included (or marked as '/') encountered GPU out-of-memory errors.

For 672-step forecasting on the SD dataset, FaST uses only 3.7GB of GPU memory (89.3% lower than GWNet's 34.5GB) with optimal training (59s/epoch) and inference times (18s). Its parameter count (709K) is higher than DLinear's 130K but less than PatchSTG's 2,421K, balancing performance and efficiency. FaST demonstrates strong scalability on the GLA dataset (672-step). Its GPU memory (17.4GB) is 38.9% lower than BigST's 28.5GB, with training time reduced to 60.5% of BigST's (514s vs 311s/epoch). The 102.7% memory growth from 96→672 step (18.8GB→38.1GB) is significantly lower than NHITS's 194.8% (13.5GB→39.8GB) and DLinear's 487.3% (5.5GB→32.3GB), validating its learning efficiency. On the CA dataset (672-step), FaST's parameter count (1,466K) exceeds most baselines but achieves competitive training (746s/epoch) and inference times (238s), outperforming BigST in training speed (746s

Table 4: Computational cost across datasets for 672-step forecasting. Notes: batch size (B.S.), GPU memory usage (G.: GB), and number of parameters (P.: K).

Method	SD			GBA			GLA			CA		
	B.S.	G.	P.									
DLinear	64	3.2	130	64	9.2	130	64	14.7	130	64	32.3	130
NHITS	64	3.8	1,344	64	11.3	1,344	64	17.9	1,344	64	39.8	1,344
CycleNet	64	3.3	463	64	9.5	620	64	15.1	762	64	33.2	1,220
STGCN	64	38.8	1,968	32	41.1	2,806	/	/	/	/	/	/
GWNet	32	34.5	888	/	/	/	/	/	/	/	/	/
SGP	64	6.8	999	/	/	/	/	/	/	/	/	/
STDMAE	32	46.1	1,250	/	/	/	/	/	/	/	/	/
BigST	64	5.7	265	64	17.8	317	64	28.5	364	32	30.9	517
STID	64	3.5	366	64	10.4	471	64	16.6	566	64	36.7	871
RPMixer	64	4.3	1,686	/	/	/	/	/	/	/	/	/
STPGNN	32	32.9	762	/	/	/	/	/	/	/	/	/
PatchSTG	64	8.6	2,421	64	33.9	3,291	64	32.1	1,798	32	42.3	1,951
FaST	64	3.7	709	64	10.9	866	64	17.4	1,008	64	38.1	1,466

†Methods not included (or marked as '/') encountered GPU out-of-memory errors.

vs 1,284s/epoch) and inference (238s vs 374s). Moreover, the memory growth rate from 96→672 steps (102.7%) and training time increase (269%) are lower than comparable models, confirming strong adaptability to long-sequence tasks.

In summary, FaST delivers an efficient solution for large-scale time series prediction. By leveraging adaptive agent attention and parallelized expert routing, it achieves high performance with minimal computational overhead. Crucially, its efficiency scales linearly with the number of graph nodes and the length of the horizon, as demonstrated in Figure 6.

4.6 Visualization Analysis

This section will demonstrate the correlation between traffic patterns and expert weight distribution through case studies. Using Node 6, Node 7, and Node 710 from the SD dataset as examples, Figure 7a illustrates the cyclical patterns in their time series, while Figure 7b displays the distribution of expert weights in the MoE module without HA-Router for these nodes, and Figure 7c displays the weight distribution in the MoE module for these nodes.

The vanilla MoE module without the HA-Router mechanism suffers from *polarization phenomena*: the majority of weights become randomly concentrated on a single expert. This incurs significant load imbalance and renders routing ineffective. In contrast, the module equipped with the HA-Router mechanism successfully mitigates these adverse effects, avoiding polarization. Concretely speaking, starting with a horizontal analysis, Node 6 and Node 7, being neighbors, exhibit similar time-series trends, while Node 710 shows a significantly different distribution. Consequently, the expert weights learned for Node 6 and Node 7 are highly consistent: Expert 0 has the largest weight, while Experts 1 and 7 have the smallest and second-smallest weights, respectively. In contrast, the weights for Node 710 are distinctly different. Moving to a longitudinal analysis, slight differences exist between the time-series distributions of Node 6 and Node 7, which are also reflected in the expert weights learned by our model. This shows that the MoE module adapts to the data schema, capturing long-term temporal patterns and spatial heterogeneity among nodes.

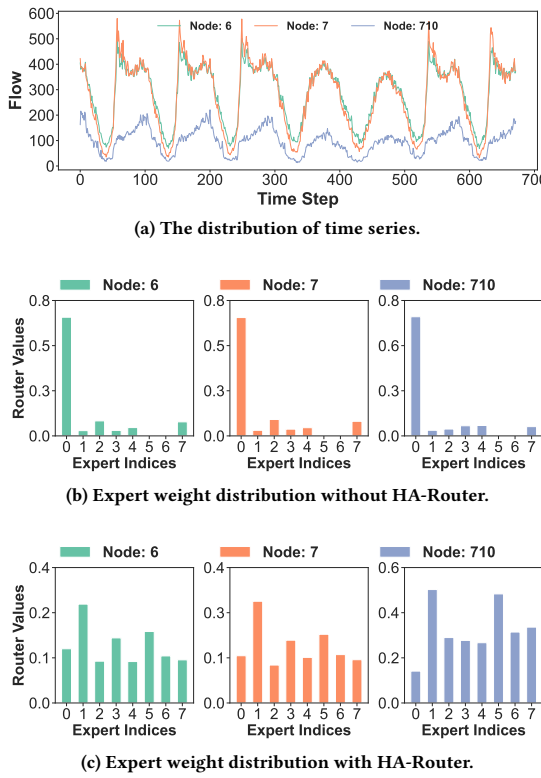


Figure 7: Visualization of expert weight distribution on the SD dataset. The routing distribution generated by HA-Router achieves load balancing.

5 Related Work

Spatial-Temporal Graph Forecasting Methods. Early efforts [26, 46] utilize GCNs to capture the spatial correlations, and RNNs or CNNs to model temporal dependencies. Follow-up studies introduce various enhancements, including adaptive graph learning [1, 43, 44], dynamic graph learning [14, 15, 22, 50], spatial-temporal synchronization learning [24, 40, 49], pre-training enhanced methods [13], embedding-based methods [29, 37], and neural ODEs [12], to better capture complex spatial and temporal dependencies. These models achieve excellent short-term accuracy (e.g., 12-step) on graphs of a few hundred nodes, but their spatial and temporal modules suffer from quadratic complexity, resulting in excessive memory and time consumption. To address scalability, structure-aware approaches (e.g., SGP [7], PatchSTG [11]) reduce spatial interactions via sparse aggregation or partitioning, yet often sacrifice long-range dependencies and rely on accurate graph structures. Conversely, structure-free methods (e.g., BigST [17], RPMixer [45], STID [37]) simplify spatial modeling with node embeddings and feature mixing, but may dilute critical spatial semantics. These limitations hinder their effectiveness in large-scale, long-horizon STG forecasting, where preserving rich spatial relationships is essential. To this end, this paper aims to simultaneously improve the accuracy and efficiency of STG in long-term and large-scale prediction.

Temporal Forecasting Methods. STG forecasting can be simplified to a time series forecasting problem by ignoring spatial information. The long-horizon forecasting challenge is tackled by Transformer variants [30, 33, 34, 51], lightweight MLP-mixers [5, 41] and linear pattern decomposition [3, 28, 47]. These temporal models lack mechanisms to encode dynamic spatial correlations, limiting their applicability to STG forecasting where joint spatial-temporal modeling is essential.

Mixture-of-Experts for Spatial-Temporal Modeling. MoE models [18] have emerged as a promising paradigm for achieving high model capacity with reduced computation via expert sparsity and input-dependent routing. Although classical MoE architectures were initially developed for static inputs and classification tasks, recent work has extended MoE to time series [4, 31, 39], where expert specialization and temporal abstraction enable efficient sequence modeling. In spatiotemporal domains, methods like ST-MoE [25] and TESTAM [23] apply MoE principles to traffic and weather data, but often rely on sparse gating with limited parallelism. Furthermore, most existing MoE applications overlook the heterogeneity and non-uniform dynamics intrinsic to large-scale urban sensing systems, where different nodes exhibit diverse temporal patterns and interaction semantics. Another challenge is expert load balancing: uneven expert selection leads to polarization, deteriorating both efficiency and accuracy. Addressing this issue is particularly important in dense MoE setups.

6 Conclusion

In this paper, we proposed FaST, an efficient framework for large-scale long-horizon spatial-temporal forecasting. By integrating a temporal compression input with MoE module, an adaptive graph agent attention mechanism, and a parallelized GLU-MoE module, FaST effectively addresses the challenges of forecasting one week ahead with thousands of nodes. The temporal compression input with MoE module extracts heterogeneous features while maintaining scalability, and the adaptive graph agent attention mechanism reduces spatial interaction complexity from quadratic to linear. The parallelized GLU-MoE module further ensures efficient feature extraction with minimal computational overhead. Extensive experiments demonstrate that FaST achieves superior long-horizon forecasting performance and significantly improves computational efficiency compared to state-of-the-art models. In future work, we plan to explore the integration of time series foundation models to further enhance the framework’s capabilities and scalability.

Acknowledgments

This work is supported by the National Natural Science Foundation of China (No. 62362069), partially supported by the Yunnan Fundamental Research Projects (No. 202401BF070001-024); the Open Fund of Beijing Key Laboratory of Traffic Data Mining and Embodied Intelligence; and the Open Project Program of Yunnan Key Laboratory of Intelligent Systems and Computing (No. ISC24Y05).

References

- [1] LEI BAI, Lina Yao, Can Li, Xianzhi Wang, and Can Wang. 2020. Adaptive Graph Convolutional Recurrent Network for Traffic Forecasting. In *Adv. Neural Inf. Process. Syst. (NeurIPS)*, H. Larochelle, M. Ranzato, R. Hadsell, M.F. Balcan, and H. Lin (Eds.), Vol. 33. 17804–17815.
- [2] Weilin Cai, Juyong Jiang, Fan Wang, Jing Tang, Sunghun Kim, and Jiayi Huang. 2025. A Survey on Mixture of Experts in Large Language Models. *IEEE Trans. Knowl. Data Eng.* 37, 7 (2025), 1–20.
- [3] Cristian Challu, Kin G. Olivares, Boris N. Oreshkin, Federico Garza Ramírez, Max Mergenthaler Canseco, and Artur Dubrawski. 2023. NHITS: Neural Hierarchical Interpolation for Time Series Forecasting. In *Proc. AAAI Conf. Artif. Intell. (AAAI)*. 6989–6997.
- [4] Peng Chen, Yingying Zhang, Yunyao Cheng, Yang Shu, Yihang Wang, Qingsong Wen, Bin Yang, and Chenjuan Guo. 2024. Pathformer: Multi-scale Transformers with Adaptive Pathways for Time Series Forecasting. In *Proc. Int. Conf. Learn. Represent. (ICLR)*. 1–19.
- [5] Si-An Chen, Chun-Liang Li, Sercan Ö. Arik, Nathanael C. Yoder, and Tomas Pfister. 2023. TSMixer: An All-MLP Architecture for Time Series Forecasting. *Trans. Mach. Learn. Res.* 2023 (2023), 1–24.
- [6] Zixiang Chen, Yihe Deng, Yue Wu, Quanquan Gu, and Yuanzhi Li. 2022. Towards Understanding the Mixture-of-Experts Layer in Deep Learning. In *Adv. Neural Inf. Process. Syst. (NeurIPS)*, Vol. 35. 23049–23062.
- [7] Andrea Cini, Ivan Marisca, Filippo Maria Bianchi, and Cesare Alippi. 2023. Scalable Spatiotemporal Graph Neural Networks. In *Proc. AAAI Conf. Artif. Intell. (AAAI)*. 7218–7226.
- [8] Yann N. Dauphin, Angela Fan, Michael Auli, and David Grangier. 2017. Language Modeling with Gated Convolutional Networks. In *Proc. Int. Conf. Mach. Learn. (ICML)*. 933–941.
- [9] Petros Drineas, Michael W Mahoney, and Nello Cristianini. 2005. On the Nyström Method for Approximating a Gram Matrix for Improved Kernel-Based Learning. *J. Mach. Learn. Res.* 6, 12 (2005).
- [10] Carl Eckart and Gale Young. 1936. The approximation of one matrix by another of lower rank. *Psychometrika* 1, 3 (1936), 211–218.
- [11] Yuchen Fang, Yuxuan Liang, Bi Hui, Zehui Shao, Liwei Deng, Xu Liu, Xinkie Jiang, and Kai Zheng. 2025. Efficient Large-Scale Traffic Forecasting with Transformers: A Spatial Data Management Perspective. In *Proc. ACM SIGKDD Int. Conf. Knowl. Discov. Data Min. (KDD)*. 307–317.
- [12] Zheng Fang, Qingqing Long, Guojie Song, and Kunqing Xie. 2021. Spatial-Temporal Graph ODE Networks for Traffic Flow Forecasting. In *Proc. ACM SIGKDD Int. Conf. Knowl. Discov. Data Min. (KDD)*. 364–373.
- [13] Haotian Gao, Renhe Jiang, Zheng Dong, Jinliang Deng, Yuxin Ma, and Xuan Song. 2024. Spatial-Temporal-Decoupled Masked Pre-Training for Spatiotemporal Forecasting. In *Proc. Int. Joint Conf. Artif. Intell. (IJCAI)*. 3998–4006.
- [14] Shengnan Guo, Youfang Lin, Ning Feng, Chao Song, and Huaiyu Wan. 2019. Attention Based Spatial-Temporal Graph Convolutional Networks for Traffic Flow Forecasting. In *Proc. AAAI Conf. Artif. Intell. (AAAI)*. 922–929.
- [15] Shengnan Guo, Youfang Lin, Huaiyu Wan, Xiucheng Li, and Gao Cong. 2022. Learning Dynamics and Heterogeneity of Spatial-Temporal Graph Data for Traffic Forecasting. *IEEE Trans. Knowl. Data Eng.* 34, 11 (2022), 5415–5428.
- [16] Dongchen Han, Tianzhu Ye, Yizeng Han, Zhuofan Xia, Siyuan Pan, Pengfei Wan, Shiji Song, and Gao Huang. 2024. Agent Attention: On the Integration of Softmax and Linear Attention. In *Proc. Eur. Conf. Comput. Vis. (ECCV)*, Vol. 15108. 124–140.
- [17] Jindong Han, Weijia Zhang, Hao Liu, Tao Tao, Naiqiang Tan, and Hui Xiong. 2024. BigST: Linear Complexity Spatio-Temporal Graph Neural Network for Traffic Forecasting on Large-Scale Road Networks. *Proc. VLDB Endow.* 17, 5 (2024), 1081–1090.
- [18] Robert A. Jacobs, Michael I. Jordan, Steven J. Nowlan, and Geoffrey E. Hinton. 1991. Adaptive Mixtures of Local Experts. *Neural Computation* 3, 1 (1991), 79–87.
- [19] Aryan Jadon, Avinash Patil, and Shruti Jadon. 2024. A Comprehensive Survey of Regression-Based Loss Functions for Time Series Forecasting. In *Int. Conf. Data Manag. Anal. Innov. (ICDMAI)*. 117–147.
- [20] Yue Jiang, Xiucheng Li, Yile Chen, Shuai Liu, Weilong Kong, Antonis F. Lentzakis, and Gao Cong. 2024. SAGDFN: A Scalable Adaptive Graph Diffusion Forecasting Network for Multivariate Time Series Forecasting. In *Proc. Int. Conf. Data Eng. (ICDE)*. 1255–1268.
- [21] Guangyin Jin, Yuxuan Liang, Yuchen Fang, Zehui Shao, Jincai Huang, Junbo Zhang, and Yu Zheng. 2024. Spatio-Temporal Graph Neural Networks for Predictive Learning in Urban Computing: A Survey. *IEEE Trans. Knowl. Data Eng.* 36, 10 (2024), 5388–5408.
- [22] Weiyang Kong, Ziyu Guo, and Yubao Liu. 2024. Spatio-Temporal Pivotal Graph Neural Networks for Traffic Flow Forecasting. In *Proc. AAAI Conf. Artif. Intell. (AAAI)*. 8627–8635.
- [23] Hyunwook Lee and Sungahn Ko. 2024. TESTAM: A Time-Enhanced Spatio-Temporal Attention Model with Mixture of Experts. In *Proc. Int. Conf. Learn. Represent. (ICLR)*. 1–19.
- [24] Mengzhang Li and Zhanxing Zhu. 2021. Spatial-Temporal Fusion Graph Neural Networks for Traffic Flow Forecasting. In *Proc. AAAI Conf. Artif. Intell. (AAAI)*. 4189–4196.
- [25] Shuhao Li, Yue Cui, Yan Zhao, Weidong Yang, Ruiyuan Zhang, and Xiaofang Zhou. 2023. ST-MoE: Spatio-temporal Mixture-of-Experts for Debiasing in Traffic Prediction. In *Proc. ACM Int. Conf. Inf. Knowl. Manag. (CIKM)*. 1208–1217.
- [26] Yaguang Li, Rose Yu, Cyrus Shahabi, and Yan Liu. 2018. Diffusion Convolutional Recurrent Neural Network: Data-driven Traffic Forecasting. In *Proc. Int. Conf. Learn. Represent. (ICLR)*. 1–16.
- [27] Yuxuan Liang, Yutong Xia, Songyu Ke, Yiwei Wang, Qingsong Wen, Junbo Zhang, Yu Zheng, and Roger Zimmermann. 2023. AirFormer: Predicting Nationwide Air Quality in China with Transformers. In *Proc. AAAI Conf. Artif. Intell. (AAAI)*. 14329–14337.
- [28] Shengsheng Lin, Weiwei Lin, Xinyi HU, Wentai Wu, Ruichao Mo, and Haocheng Zhong. 2024. CycleNet: Enhancing Time Series Forecasting through Modeling Periodic Patterns. In *Adv. Neural Inf. Process. Syst. (NeurIPS)*, Vol. 37. 106315–106345.
- [29] Hangchen Liu, Zheng Dong, Renhe Jiang, Jiewen Deng, Jinliang Deng, Quanjun Chen, and Xuan Song. 2023. Spatio-Temporal Adaptive Embedding Makes Vanilla Transformer SOTA for Traffic Forecasting. In *Proc. ACM Int. Conf. Inf. Knowl. Manag. (CIKM)*. 4125–4129.
- [30] Shizhan Liu, Hang Yu, Cong Liao, Jianguo Li, Weiyao Lin, Alex X. Liu, and Schahram Dustdar. 2022. Pyraformer: Low-complexity Pyramidal Attention for Long-Range Time Series Modeling and Forecasting. In *Proc. Int. Conf. Learn. Represent. (ICLR)*. 1–20.
- [31] Xu Liu, Juncheng Liu, Gerald Woo, Taha Aksu, Yuxuan Liang, Roger Zimmermann, Chenghao Liu, Silvio Savarese, Caiming Xiong, and Doyen Sahoo. 2024. Moirai-MoE: Empowering Time Series Foundation Models with Sparse Mixture of Experts. *arXiv preprint arXiv:2410.10469* (2024). arXiv:2410.10469
- [32] Xu Liu, Yutong Xia, Yuxuan Liang, Junfeng Hu, Yiwei Wang, Lei Bai, Chao Huang, Zhengguang Liu, Bryan Hooi, and Roger Zimmermann. 2023. LargeST: A Benchmark Dataset for Large-Scale Traffic Forecasting. In *Adv. Neural Inf. Process. Syst. (NeurIPS)*, Vol. 36. 75354–75371.
- [33] Yong Liu, Tengge Hu, Haoran Zhang, Haixu Wu, Shiyu Wang, Lintao Ma, and Mingheng Long. 2024. ITformer: Inverted Transformers Are Effective for Time Series Forecasting. In *Proc. Int. Conf. Learn. Represent. (ICLR)*. 1–25.
- [34] Yuqi Nie, Nam H. Nguyen, Phanwadee Sinthong, and Jayant Kalagnanam. 2023. A Time Series Is Worth 64 Words: Long-term Forecasting with Transformers. In *Proc. Int. Conf. Learn. Represent. (ICLR)*. 1–24.
- [35] Saeed Rahmani, Asiyeh Baghban, Nizar Bouguila, and Zachary Patterson. 2023. Graph Neural Networks for Intelligent Transportation Systems: A Survey. *IEEE Trans. Intell. Transp. Syst.* 24, 8 (2023), 8846–8885.
- [36] Zehui Shao, Fei Wang, Yongjun Xu, Wei Wei, Chengqing Yu, Zhao Zhang, Di Yao, Tao Sun, Guangyin Jin, Xin Cao, et al. 2024. Exploring progress in multivariate time series forecasting: Comprehensive benchmarking and heterogeneity analysis. *IEEE Trans. Knowl. Data Eng.* 37, 1 (2024), 291–305.
- [37] Zehui Shao, Zhao Zhang, Fei Wang, Wei Wei, and Yongjun Xu. 2022. Spatial-Temporal Identity: A Simple yet Effective Baseline for Multivariate Time Series Forecasting. In *Proc. ACM Int. Conf. Inf. Knowl. Manag. (CIKM)*. 4454–4458.
- [38] Noam Shazeer, Azalia Mirhoseini, Krzysztof Maziarz, Andy Davis, Quoc V. Le, Geoffrey E. Hinton, and Jeff Dean. 2017. Outrageously Large Neural Networks: The Sparsely-Gated Mixture-of-Experts Layer. In *Proc. Int. Conf. Learn. Represent. (ICLR)*. 1–19.
- [39] Xiaoming Shi, Shiyu Wang, Yuqi Nie, Dianqi Li, Zhou Ye, Qingsong Wen, and Ming Jin. 2025. Time-MoE: Billion-scale Time Series Foundation Models with Mixture of Experts. In *Proc. Int. Conf. Learn. Represent. (ICLR)*. 1–33.
- [40] Chao Song, Youfang Lin, Shengnan Guo, and Huaiyu Wan. 2020. Spatial-Temporal Synchronous Graph Convolutional Networks: A New Framework for Spatial-Temporal Network Data Forecasting. In *Proc. AAAI Conf. Artif. Intell. (AAAI)*. 914–921.
- [41] Shiyu Wang, Haixu Wu, Xiaoming Shi, Tengge Hu, Huakun Luo, Lintao Ma, James Y. Zhang, and Jun Zhou. 2024. TimeMixer: Decomposable Multiscale Mixing for Time Series Forecasting. In *Proc. Int. Conf. Learn. Represent. (ICLR)*. 1–27.
- [42] Christopher Williams and Matthias Seeger. 2000. Using the Nyström method to speed up kernel machines. In *Adv. Neural Inf. Process. Syst. (NeurIPS)*, Vol. 13. 1–7.
- [43] Zonghan Wu, Shirui Pan, Guodong Long, Jing Jiang, Xiaojun Chang, and Chengqi Zhang. 2020. Connecting the Dots: Multivariate Time Series Forecasting with Graph Neural Networks. In *Proc. ACM SIGKDD Int. Conf. Knowl. Discov. Data Min. (KDD)*. 753–763.
- [44] Zonghan Wu, Shirui Pan, Guodong Long, Jing Jiang, and Chengqi Zhang. 2019. Graph WaveNet for Deep Spatial-Temporal Graph Modeling. In *Proc. Int. Joint Conf. Artif. Intell. (IJCAI)*. 1907–1913.
- [45] Chin-Chia Michael Yeh, Yujie Fan, Xin Dai, Uday Singh Saini, Vivian Lai, Prince Osei Aboagye, Junpeng Wang, Huiyuan Chen, Yan Zheng, Zhongfang Zhuang, Liang Wang, and Wei Zhang. 2024. RPMixer: Shaking up Time Series Forecasting with Random Projections for Large Spatial-Temporal Data. In *Proc. ACM SIGKDD Int. Conf. Knowl. Discov. Data Min. (KDD)*. 3919–3930.
- [46] Bing Yu, Haoteng Yin, and Zhanxing Zhu. 2018. Spatio-Temporal Graph Convolutional Networks: A Deep Learning Framework for Traffic Forecasting. In *Proc.*

Int. Joint Conf. Artif. Intell. (IJCAI). 3634–3640.

[47] Ailing Zeng, Muxi Chen, Lei Zhang, and Qiang Xu. 2023. Are Transformers Effective for Time Series Forecasting?. In *Proc. AAAI Conf. Artif. Intell. (AAAI)*. 11121–11128.

[48] Biao Zhang and Rico Sennrich. 2019. Root Mean Square Layer Normalization. In *Adv. Neural Inf. Process. Syst. (NeurIPS)*. 12360–12371.

[49] Yiji Zhao, Youfang Lin, Haomin Wen, Tonglong Wei, Xiyuan Jin, and Huaiyu Wan. 2023. Spatial-Temporal Position-Aware Graph Convolution Networks for Traffic Flow Forecasting. *IEEE Trans. Intell. Transp. Syst.* 24, 8 (2023), 8650–8666.

[50] Chuapan Zheng, Xiaoliang Fan, Cheng Wang, and Jianzhong Qi. 2020. GMAN: A Graph Multi-Attention Network for Traffic Prediction. In *Proc. AAAI Conf. Artif. Intell. (AAAI)*. 1234–1241.

[51] Haoyi Zhou, Shanghang Zhang, Jieqi Peng, Shuai Zhang, Jianxin Li, Hui Xiong, and Wancai Zhang. 2021. Informer: Beyond Efficient Transformer for Long Sequence Time-Series Forecasting. In *Proc. AAAI Conf. Artif. Intell. (AAAI)*. 11106–11115.

[52] Yanqi Zhou, Tao Lei, Hanxiao Liu, Nan Du, Yanping Huang, Vincent Y. Zhao, Andrew M. Dai, Zhifeng Chen, Quoc V. Le, and James Laudon. 2022. Mixture-of-Experts with Expert Choice Routing. In *Adv. Neural Inf. Process. Syst. (NeurIPS)*. Vol. 35. 7103–7114.

A Theoretical Analysis of AGA-Att Fidelity

A.1 Spatial Reconstruction Error

AGA-Att can be interpreted as a lossy low-rank projection that compresses node interactions through $a \ll N$ agent tokens. For a focused analysis of spatial compression, we ignore the value projection \mathbf{W}_V^ℓ (which mainly serves as a learned feature transform) and consider the effective projection:

$$\mathbf{P}^\ell = \mathbf{A}_{\text{dist}}^\ell \mathbf{A}_{\text{agg}}^\ell \in \mathbb{R}^{N \times N}. \quad (17)$$

We can define the normalized reconstruction error at layer ℓ as

$$\epsilon^\ell = \frac{\|\mathbf{H}_t^{\ell-1} - \mathbf{P}^\ell \mathbf{H}_t^{\ell-1}\|_F}{\|\mathbf{H}_t^{\ell-1}\|_F}, \quad (18)$$

which measures how well AGA-Att preserves the input features after spatial compression. Since AGA-Att maps node features to a agent tokens and back, $\text{rank}(\mathbf{P}^\ell \mathbf{H}_t^{\ell-1}) \leq a$ holds, implying a rank- a approximation effect.

A.2 Fidelity Bounds: Lower and Upper Bounds

Lower bound. Let the singular value decomposition of $\mathbf{H}_t^{\ell-1} \in \mathbb{R}^{N \times d}$ be $\mathbf{H}_t^{\ell-1} = \mathbf{U} \mathbf{\Sigma} \mathbf{V}^\top$, with singular values $\sigma_1 \geq \dots \geq \sigma_{\min(N,d)}$. By the Eckart–Young–Mirsky theorem [10], any rank- a approximation $\hat{\mathbf{H}}$ satisfies $\|\mathbf{H}_t^{\ell-1} - \hat{\mathbf{H}}\|_F \geq \sqrt{\sum_{i=a+1}^{\min(N,d)} \sigma_i^2}$. Since $\mathbf{P}^\ell \mathbf{H}_t^{\ell-1}$ has rank at most a , we obtain

$$\epsilon^\ell \geq \frac{\sqrt{\sum_{i=a+1}^{\min(N,d)} \sigma_i^2}}{\|\mathbf{H}_t^{\ell-1}\|_F}. \quad (19)$$

This bound characterizes the *minimum* information loss incurred by any rank- a projection.

Upper bound. AGA-Att is closely related to Nyström-style kernel approximation, where agent tokens act as inducing points [9, 42]. Let $\mathbf{K} = \mathbf{H}_t^{\ell-1} (\mathbf{H}_t^{\ell-1})^\top$ be the Gram matrix with eigenvalues $\lambda_1 \geq \dots \geq \lambda_N$. A Nyström approximation typically yields an expected error bounded by the optimal rank- a residual plus a sampling term that decays with a . Adapting this to our projection view gives:

$$\mathbb{E}[\epsilon^\ell] \leq \frac{\sqrt{\sum_{i=a+1}^N \lambda_i^2}}{\|\mathbf{H}_t^{\ell-1}\|_F} + O\left(\frac{1}{\sqrt{a}}\right), \quad (20)$$

suggesting improved fidelity with more agent tokens.

A.3 Empirical Reconstruction Errors

Table 5 reports reconstruction errors on the SD dataset under $96 \Rightarrow 48$ forecasting while varying the number of agent tokens $a \in \{16, 32, 64, 128\}$. For the first layer, ϵ^1 decreases monotonically as a increases, indicating that early-layer representations contain strong shared spatial modes that can be captured by more agents. To reflect the cumulative effect across layers, we compute the average reconstruction error ϵ_{avg} over all layers, which attains its minimum at $a = 32$. Across the four settings, ϵ_{avg} exhibits strong positive correlation with forecasting errors: Pearson correlation coefficients are 0.929 ($p=0.071$) with MAE and 0.955 ($p=0.045$) with RMSE, implying that higher fidelity (lower ϵ_{avg}) is associated with better predictive accuracy. Overall, reconstruction errors remain below 0.75, indicating that the approximation is sufficiently faithful for downstream forecasting while enabling scalable computation.

Table 5: Reconstruction errors on SD ($96 \Rightarrow 48$) with different numbers of agent tokens a . Lower is better for ϵ .

#Agent	$a=16$	$a=32$	$a=64$	$a=128$
ϵ^1 ($\ell=1$)	0.611	0.512	0.488	0.484
ϵ^2 ($\ell=2$)	0.617	0.685	0.726	0.755
ϵ^3 ($\ell=3$)	0.652	0.663	0.677	0.665
ϵ_{avg}	0.627	0.620	0.630	0.632
MAE	19.75	19.37	20.02	19.87
RMSE	35.22	34.54	36.27	36.23

B Short-Horizon Forecasting Performance

To evaluate short-horizon forecasting performance, we report results under the $96 \Rightarrow 12$ setting on SD, GBA, GLA, and CA in Table 6. FaST achieves the best performance across all datasets. In particular, it improves MAPE by 5.47% to 11.2% relative to the strongest baseline, while the relative gains on the other metrics are generally smaller than those observed in long-horizon forecasting.

C Generalization to Other Domains

FaST naturally extends, replacing traffic flows with variables such as electricity demand, precipitation, or temperature. Similar to traffic data, power demand datasets often exhibit high spatial redundancy (e.g., power stations across a region) and temporal heterogeneity (e.g., daily load cycles, seasonal trends). FaST can be applied to power demand forecasting, where the model captures both the spatial correlations between power stations and the temporal dynamics of energy consumption.

To assess generalization beyond the LargeST benchmarks, we additionally evaluate FaST on the Electricity (power demand) dataset, which contains 321 variables sampled at 1-hour intervals over 2012–2014. The dataset comprises 8.38M–8.43M samples with mean 2,538.79 and standard deviation 15,027.57. Under the 24-step input to $\{12, 24, 48, 168\}$ -step output setting, Table 7 shows that FaST consistently achieves the best predictive accuracy, improving MAPE by 12.03%–19.06% over the strongest baseline.

Table 6: Performance comparisons. Bold indicates first place, underline indicates second place. "96=>48" denotes training on the past 96 time steps to predict the next 48. Missing entries or '/' on GBA, GLA and CA datasets indicate out-of-memory errors.

Data	Method	96=>12				96=>48				96=>96				96=>192				96=>672			
		MAE	RMSE	MAPE	R ²	MAE	RMSE	MAPE	R ²	MAE	RMSE	MAPE	R ²	MAE	RMSE	MAPE	R ²	MAE	RMSE	MAPE	R ²
SD	DLinear	28.32	49.90	17.57%	0.9256	36.64	65.20	23.29%	0.8731	38.42	68.03	23.72%	0.8623	45.95	78.12	29.04%	0.8134	46.78	80.44	31.39%	0.8093
	NHITS	19.95	33.31	12.55%	0.9670	26.32	45.52	17.46%	0.9369	29.13	50.84	19.44%	0.9201	34.55	58.17	23.22%	0.8993	38.10	64.32	26.16%	0.8780
	CycleNet	20.28	33.71	14.17%	0.9653	25.40	43.07	18.66%	0.9422	27.28	46.36	20.16%	0.9323	32.14	53.63	24.36%	0.9144	34.80	58.26	25.92%	0.9000
	DCRNN	20.79	33.31	14.47%	0.9668	33.23	53.54	23.22%	0.8932	42.19	65.36	27.53%	0.8577	/	/	/	/	/	/	/	/
	STGCN	17.69	31.81	12.38%	0.9698	22.52	41.04	16.27%	0.9498	25.50	45.73	18.66%	0.9377	30.27	53.16	22.11%	0.9159	35.54	61.31	25.66%	0.8892
	GWNet	16.94	28.33	11.25%	0.9759	20.98	36.01	14.15%	<u>0.9613</u>	22.86	40.29	16.04%	0.9517	25.41	45.90	17.88%	0.9373	28.86	53.07	20.94%	0.9170
	SGP	20.52	35.59	12.84%	0.9671	29.54	54.40	21.41%	0.9107	33.71	61.54	23.51%	0.8946	38.67	70.88	25.67%	0.8815	41.32	71.92	27.84%	0.8425
	STPGNN	17.65	29.31	11.42%	0.9742	24.01	40.85	16.55%	0.9502	24.48	45.27	17.10%	0.9390	27.70	51.64	19.19%	0.9206	35.78	60.36	26.57%	0.8926
	STDMAE	<u>16.14</u>	<u>27.12</u>	<u>10.60%</u>	<u>0.9779</u>	21.45	37.60	14.71%	0.9578	24.48	45.27	17.10%	0.9390	27.70	51.64	19.19%	0.9206	32.02	59.25	21.99%	0.8965
	BigST	17.65	30.14	12.45%	0.9740	22.98	39.67	17.16%	0.9551	25.31	43.64	19.44%	0.9434	27.12	48.19	20.35%	0.9324	29.45	52.06	22.28%	0.9185
	STID	16.42	28.61	10.93%	0.9746	<u>20.82</u>	38.87	14.44%	0.9545	22.82	43.23	<u>16.04%</u>	0.9450	24.68	46.66	<u>17.48%</u>	0.9348	27.72	<u>51.65</u>	20.09%	<u>0.9235</u>
	RPMixer	17.11	28.51	11.19%	0.9743	21.60	38.90	14.66%	0.9538	23.59	42.54	16.17%	0.9348	25.72	46.22	18.31%	0.9255	28.26	52.74	20.08%	0.9105
	PatchSTG	16.29	27.67	12.47%	0.9771	21.55	40.45	14.89%	0.9490	23.38	44.07	16.06%	0.9392	25.91	49.64	18.54%	0.9262	28.33	54.02	19.67%	0.9161
	FaST	15.77	27.09	10.02%	0.9781	19.37	34.54	12.85%	0.9644	21.46	39.18	14.37%	0.9543	24.23	45.09	16.48%	0.9395	26.56	49.26	18.08%	0.9285
	Improvement	2.29%	0.11%	5.47%	0.02%	6.96%	4.08%	9.19%	0.32%	5.96%	2.76%	10.41%	0.27%	1.82%	1.76%	5.72%	0.23%	4.18%	4.63%	8.08%	0.54%
GBA	DLinear	28.21	47.95	22.20%	0.9161	34.95	61.09	26.25%	0.8646	36.20	63.16	27.08%	0.8552	42.44	71.58	34.47%	0.8145	43.38	72.73	35.77%	0.8094
	NHITS	20.74	34.99	15.72%	0.9552	26.53	46.04	22.39%	0.9222	28.68	49.75	24.79%	0.9088	32.38	54.60	28.38%	0.8903	34.98	58.36	30.72%	0.8758
	CycleNet	21.36	35.34	17.84%	0.9538	26.19	44.51	23.10%	0.9270	27.57	46.82	24.57%	0.9197	30.19	50.47	27.80%	0.9060	32.50	53.70	29.97%	0.8911
	STGCN	20.45	34.09	16.30%	0.9575	25.78	42.24	22.47%	0.9350	28.96	47.81	25.34%	0.9170	32.38	52.33	30.21%	0.9006	35.07	56.09	31.79%	0.9006
	BigST	19.67	32.32	16.12%	0.9629	24.18	39.32	22.34%	0.9442	25.80	42.56	24.63%	0.9357	27.51	44.96	26.20%	0.9264	29.54	<u>48.03</u>	27.91%	0.9166
	STID	18.13	31.46	14.80%	<u>0.9645</u>	<u>22.31</u>	<u>39.14</u>	19.95%	<u>0.9447</u>	<u>23.65</u>	<u>41.54</u>	20.61%	<u>0.9380</u>	25.82	44.43	<u>22.32%</u>	0.9284	<u>27.83</u>	48.09	24.86%	<u>0.9195</u>
	RPMixer	18.68	31.11	14.69%	0.9623	23.73	40.65	20.09%	0.9368	24.64	42.03	20.68%	0.9330	<u>25.77</u>	<u>44.35</u>	<u>22.81%</u>	<u>0.9288</u>	/	/	/	/
	PatchSTG	<u>18.12</u>	30.59	<u>13.93%</u>	0.9641	22.40	39.23	<u>19.77%</u>	0.9426	23.76	42.45	20.45%	0.9334	26.29	46.39	22.82%	0.9221	28.40	49.94	24.58%	0.9096
	FaST	17.73	<u>30.71</u>	<u>12.37%</u>	0.9656	21.94	38.73	17.12%	0.9454	23.11	40.74	19.58%	0.9397	25.30	43.85	22.07%	0.9302	26.82	46.90	22.78%	0.9207
	Improvement	2.15%	-0.39%	11.20%	0.11%	1.66%	1.05%	13.40%	0.07%	2.28%	1.93%	4.25%	0.18%	1.82%	1.13%	1.12%	0.15%	3.63%	2.35%	7.32%	0.13%
GLA	DLinear	29.04	49.83	17.80%	0.9295	36.63	58.28	22.88%	0.8849	38.03	65.63	23.83%	0.8772	44.88	74.97	29.74%	0.8396	45.61	76.27	31.07%	0.8346
	NHITS	20.77	34.82	12.39%	0.9653	27.15	47.00	17.47%	0.9360	29.51	51.00	19.44%	0.9250	33.95	56.89	23.12%	0.9063	36.77	61.14	25.57%	0.8919
	CycleNet	21.17	35.21	14.22%	0.9638	26.50	44.81	19.34%	0.9411	28.13	47.51	20.52%	0.9350	31.55	52.11	23.96%	0.9216	33.54	55.23	25.54%	0.9113
	BigST	19.05	31.21	13.24%	0.9698	24.41	40.94	18.67%	0.9520	25.33	<u>42.62</u>	18.98%	0.9461	28.17	46.97	21.79%	<u>0.9379</u>	31.10	51.32	24.26%	0.9248
	STID	17.53	29.97	11.19%	<u>0.9741</u>	<u>22.15</u>	40.08	15.05%	0.9534	23.93	43.71	16.69%	0.9454	<u>26.16</u>	<u>46.84</u>	18.78%	0.9360	28.85	<u>51.22</u>	20.89%	<u>0.9252</u>
	RPMixer	18.48	30.15	11.50%	0.9720	23.26	<u>39.71</u>	15.78%	<u>0.9557</u>	25.34	43.17	19.15%	0.9509	/	/	/	/	/	/	/	/
	PatchSTG	<u>17.51</u>	29.79	11.03%	0.9741	22.44	40.83	14.94%	0.9530	23.91	43.42	16.42%	0.9452	26.57	48.20	18.34%	0.9345	29.33	52.69	20.67%	0.9218
	FaST	17.20	<u>29.22</u>	<u>10.27%</u>	0.9756	21.72	38.52	<u>14.12%</u>	0.9575	22.93	40.78	15.21%	0.9526	25.48	44.43	16.94%	0.9437	27.38	48.33	18.84%	0.9335
	Improvement	1.77%	1.91%	6.89%	0.15%	1.94%	3.00%	5.49%	0.19%	4.10%	4.32%	7.37%	0.18%	2.60%	5.15%	7.63%	0.62%	5.10%	5.64%	8.85%	0.90%
CA	DLinear	26.51	46.11	19.10%	0.9314	33.34	59.03	23.66%	0.8876	34.63	56.98	24.72%	0.8796	40.83	69.78	30.87%	0.8431	41.65	71.09	32.34%	0.8380
	NHITS	19.57	33.21	13.90%	0.9644	25.61	44.84	20.04%	0.9355	27.99	48.91	21.72%	0.9229	32.10	54.32	25.49%	0.9049	34.28	57.83	27.52%	0.8928
	CycleNet	19.96	33.58	15.64%	0.9636	24.69	42.37	20.69%	0.9421	26.18	44.78	22.03%	0.9353	29.27	49.10	25.34%	0.9223	31.05	51.93	26.85%	0.9136
	BigST	17.65	29.32	14.07%	0.9723	22.26	37.47	18.76%	0.9547	24.28	40.29	20.81%	0.9477	27.64	45.44	23.92%	0.9335	29.86	49.93	26.88%	0.9201
	STID	16.32	28.27	12.46%	0.9742	<u>20.58</u>	37.43	16.42%	0.9548	<u>22.07</u>	<u>40.22</u>	17.95%	<u>0.9479</u>	24.16	43.55	19.99%	0.9389	26.52	47.18	22.06%	0.9286
	RPMixer	17.33	28.51	13.37%	0.9719	21.48	<u>36.54</u>	17.09%	<u>0.9563</u>	/	/	/	/	/	/	/	/	/	/	/	/
	PatchSTG	<u>16.15</u>	<u>27.80</u>	<u>12.21%</u>	<u>0.9753</u>	20.59	37.34	<u>16.21%</u>	0.9550	22.25	41.72	<u>17.90%</u>	0.9439	24.89	46.00	20.30%	0.9318	27.54	49.77	22.67%	0.9206
	FaST	15.78	<u>27.37</u>	10.95%	0.9758	19.57	35.20	14.69%	0.9600	20.90	37.78	16.18%	0.9536	22.87	41.30	17.98%	0.9456	25.35	45.37	20.41%	0.9344
	Improvement	2.29%	1.55%	10.32%	0.05%	4.91%	3.67%	9.38%	0.39%	5.30%	6.07%	9.61%	0.60%	5.34%	5.17%	10.06%	0.71%	4.41%	3.84%	7.48%	0.62%

Table 7: Performance comparisons on the Electricity dataset (24=>12/24/48/168). Bold indicates first place, underline indicates second place. The notation "24=>12" denotes training on the past 24 time steps to predict the next 12 time steps.

Task	Metric	DLinear	NHITS	CycleNet	DCRNN	STGCN	GWNet	SGP	STPGNN	STDMAE	BigST	STID	FaST	Improv.

<tbl_r cells